Electronic and magnetic properties of single-layer MPX_3 metal phosphorous trichalcogenides

Bheema Lingam Chittari,[1,2] Youngju Park,[2] Dongkyu Lee,[2] Moonsup Han,[2] Allan H. MacDonald,[3]
Euyheon Hwang,[1,*] and Jeil Jung[2,†]

[1]*SKKU Advanced Institute of Nanotechnology, Sungkyunkwan University, Suwon 16419, Korea*
[2]*Department of Physics, University of Seoul, Seoul 02504, Korea*
[3]*Department of Physics, The University of Texas at Austin, Austin, Texas 78712, USA*

We survey the electronic structure and magnetic properties of two-dimensional (2D) MPX_3 (M = V, Cr, Mn, Fe, Co, Ni, Cu, Zn, and X = S, Se, Te) transition-metal chalcogenophosphates to shed light on their potential role as single-layer van der Waals materials that possess magnetic order. Our *ab initio* calculations predict that most of these single-layer materials are antiferromagnetic semiconductors. The band gaps of the antiferromagnetic states decrease as the atomic number of the chalcogen atom increases (from S to Se to Te), leading in some cases to half-metallic ferromagnetic states or to nonmagnetic metallic states. We find that the competition between antiferromagnetic and ferromagnetic states can be substantially influenced by gating and by strain engineering. The sensitive interdependence we find between magnetic, structural, and electronic properties establishes the potential of this 2D materials class for applications in spintronics.

I. INTRODUCTION

Following seminal studies that reported on the exfoliation of a stable single-layer graphene and on transport measurements with nearly ideal Dirac fermion fingerprints [1,2], research on ultrathin two-dimensional (2D) materials has emerged during the last decade as one of the most active research topics in condensed-matter physics. Two-dimensional materials are interesting in part because their properties can be modified *in situ* by adjusting gate voltages. Recently, the focus of 2D materials research has expanded beyond graphene to include other layered van der Waals materials with a variety of distinct physical properties [3]. For example, one popular class of 2D materials is the transition-metal dichalcogenides (TMDCs) [4] which includes metals, semiconductors with exceptionally strong light-matter coupling [5], and broken symmetry electronic states, including ones with charge density wave and superconducting order [6–10]. Magnetic order has, however, not yet been established in any two-dimensional material. Room-temperature magnetism in a single-layer material is an extremely attractive material target because of the expectation that it might provide unprecedented electrical control of magnetism and enable new classes of information processing devices that incorporate nonvolatile memory elements more intimately.

One strategy to search theoretically for magnetism in isolated two-dimensional van der Waals materials is to explore the magnetic properties of single layers exfoliated from a bulk material that exhibits robust magnetic order. Following this approach, recent theoretical studies have proposed a number of potential magnetic single-layer van der Waals materials, including group-V-based dichalcogenides [11], FeBr$_3$, the chromium-based ternary tritellurides CrSiTe$_3$ and CrGeTe$_3$ [12–19], CrX$_3$ trihalides [20,21], and MnPX_3 ternary chalcogenides [22,23]. The vanadium-based dichalcogenides,

VX_2 (X = S, Se), were proposed first and are predicted to have strain-tunable ferromagnetic phases [11]. The trihalides CrX_3 (X = F, Cl, Br, I) [21] are new classes of semiconducting ferromagnets with Curie temperature predictions of T_C < 100 K.

The bulk ternary tritellurides CrATe$_3$ (A = Si, Ge) [13] were predicted within local density approximation (LDA) to be ferromagnetic with small band gaps of 0.04 and 0.06 eV, respectively. Their few-layer limits have recently been studied in temperature-dependent transport experiments [14]. The anisotropy along the c axis and the dynamic correlations in the ab plane seen by elastic and inelastic neutron scattering are characteristic of 2D magnetism [15]. In the single-layer limit, CrSiTe$_3$ is a semiconductor with a generalized gradient approximation (GGA) gap of 0.4 eV [16], substantially larger than its bulk value, and has a negative thermal expansion [17]. Reports differ on the most stable magnetic phase between ferromagnetic [13,16,17] and antiferromagnetic [18]. For larger atomic number compounds such as CrGeTe$_3$ and CrSnTe$_3$, density functional theory (DFT) predicts ferromagnetic semiconducting phases with Curie temperatures between 80–170 K [14,18,19].

We focus here on single-layer materials formed from compounds in the transition-metal phosphorous trichalcogenide (MPX_3) family, which are known to exhibit magnetism for M = Mn and for a number of other metal atom species. Metal phosphorous trichalcogenides are cousins of CrSiTe$_3$, but are so far less studied for 2D magnetism. According to one recent study, monolayer MnPSe$_3$ and MnPS$_3$ exhibit Neel antiferromagnetism [22] and valley-dependent optical properties [23]. The structures and magnetic properties of some bulk compounds from this family have already been extensively studied [24–49]. Because of the van der Waals (vdW) character of these materials, one focus of bulk materials research is to characterize ion intercalation properties [50–54]. For 2D magnetic materials to be most useful in device applications, it is desirable to seek pathways to increase the critical temperature at which they order magnetically. We compare theoretical predictions for a variety of late 3d

*euyheon@skku.edu
†jeiljung@uos.ac.kr

transition metals (M = V, Cr, Mn, Fe, Co, Ni, Cu, Zn) and consider all three chalcogen atoms (X = S, Se, Te) in an effort to explore the magnetic phases that can be expected as fully as possible. We study how the electronic bands are modified when the magnetic state undergoes a transition from antiferromagnetic to ferromagnetic, or from magnetic to nonmagnetic. Our results confirm the expected strong interdependence between magnetism and structural properties, for example lattice constant and crystal symmetry, and explain a surprisingly strong dependence of exchange interaction strengths on electron density and strain. Because these materials may have relatively strong correlations, *ab initio* density functional theory is not able to make quantitatively reliable predictions for all properties. Nevertheless, our survey provides considerable insight into materials-property trends, and into the potential for engineering the magnetic properties of these materials using field effects and strain engineering.

Our paper is structured in the following manner. We start in Sec. II by briefly summarizing some specific details of our first-principles electronic structure calculations. In Sec. III, we discuss our results for ground-state properties, including structure, magnetic properties, electronic band structures, and densities of states. Section IV is devoted to an analysis of the carrier-density dependence of the magnetic ground state, and to a study of the influence of strain on the magnetic phase diagram. Finally, we close the paper in Sec. V with a summary and discussion of our results.

II. *AB INITIO* CALCULATION DETAILS

The study of the ground-state electronic structure and magnetic properties in this work has been carried out using plane-wave density functional theory as implemented in QUANTUM ESPRESSO [55]. We have used the Rappe-Rabe-Kaxiras-Joannopoulos ultrasoft (RRKJUS) pseudopotentials for the semilocal Perdew-Burke-Ernzerhof (PBE) generalized gradient approximation (GGA) [56] together with the vdW-D2 correction [57]. We choose the GGA+D2 as a reference calculation because of the overall improvement of the GGA over the LDA [58] for a covalent bond description, and add the longer-ranged D2 correction to improve the description of binding between the layers. (The GGA typically performs poorly for van der Waals bonds [59].) The magnetic solutions have also been compared with calculations employing the DFT+U scheme, using the same value of $U = 4$ eV and alternatively using on-site repulsion U values that saturate the magnitude of the band gap. Comparisons were made with hybrid Heyd-Scuseria-Ernzerhof (HSE)+D2 functionals [60] to assess nonlocal exchange effects that could further influence the magnetic ground states. All structures were optimized without constraints until the forces on each atom reached 10^{-5} Ry/au. The self-consistency criteria for total energies has been set at 10^{-10} Ry and momentum-space integrals were performed using a regularly spaced k-point sampling density of $16 \times 16 \times 1$ for the triangular lattice case and $16 \times 8 \times 1$ for the rectangular lattice case, with a plane-wave energy cutoff between 60 to 90 Ry. For the HSE+D2 calculation, we used a coarser effective k-point sampling of $4 \times 4 \times 1$. The out-of-plane vertical size of the periodic supercell was chosen to be 25 Å,

which typically leaves an adequate vacuum spacing greater than 10 Å between two-dimensional layers.

III. STRUCTURAL AND MAGNETIC PROPERTIES

The atomic structure of MPX_3 transition-metal chalcogenophosphate layers is anchored by $(P_2X_6)^{4-}$ bipyramids arranged in a triangular lattice that provide enclosures for transition-metal atoms. (See Fig. 1 for a schematic illustration of the single-layer unit cell and the bulk atomic structure.) The bulk crystals consist of ABC-stacked single-layer assemblies that are held together by van der Waals forces. Although the atomic structures of single-layer
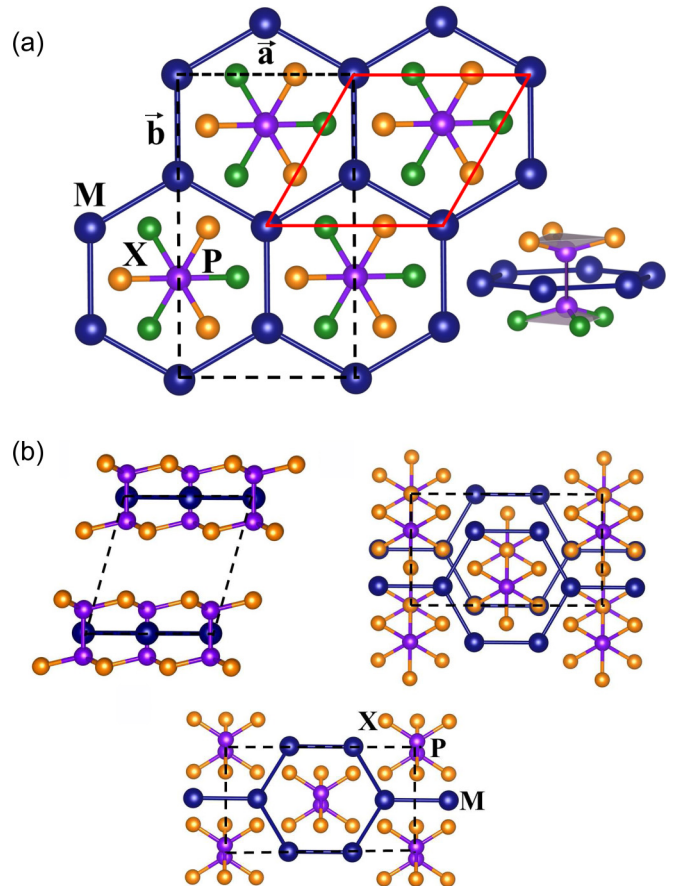

FIG. 1. Schematic structure of the transition-metal phosphorous trichalcogenide MPX_3 compounds with $(P_2X_6)^{4-}$ bipyramids that enclose metal atoms. (a) Atomic structure of a MPX_3 monolayer. The rectangular supercell referred to in the main text is indicated by black dashed lines and the smaller triangular lattice unit cell is represented by red solid lines. Each triangular unit cell contains a transition-metal atom (M) honeycomb sublattice. The phosphorus (P) dimers are perpendicular to the plane at the center of each honeycomb lattice hexagon, and three sulfur atoms are bound to each of the P atoms. The top and bottom chalcogen trimers have a relative in-plane twist of 60 degrees. (b) The lowest-energy 3D-bulk structure consists of individual layers stacked in an ABC sequence. We present the structure from three viewpoints, i.e., a side view, a top view in which the phosphorous atoms within a single layer lie on top of each other, and a view in which the transition-metal atoms of adjacent layers lie on top of each other.

transition-metal phosphorous trichalcogenide crystals are similar to those of bulk crystals, small changes appear in response to the absence of the interlayer coupling, with distortions in the ground-state crystal geometries correlated mainly with the magnetic phase. The analysis of magnetic properties is simplified by the fact that the magnetic moments develop almost entirely at the metal atom sites.

We calculate the magnetic ground-state and metastable magnetic configurations by identifying the energy extrema obtained by iterating self-consistent field equations to convergence starting from magnetic initial conditions that can be classified as either Néel antiferromagnetic (AFM), ferromagnetic (FM), or nonmagnetic (NM) states. The calculation indicates that most 2D MPX_3 crystals are semiconductors with localized magnetic moments that are ordered antiferromagnetically. We find that the use of chalcogen atoms with larger atomic numbers tends to yield smaller energy gaps between valence and conduction bands. In the following, we present an analysis of the structural and magnetic properties of representative $3d$ transition-metal MPX_3 trichalcogenides, and discuss their underlying electronic band structures.

A. Structural properties

The MPX_3 compounds that we study consist of V, Cr, Mn, Fe, Co, Ni, Cu, and Zn transition-metal atoms with $3d$ valence electrons, combined with three different chalcogen atoms S, Se, and Te. We thus expand our study beyond the most common crystals in this class, i.e., the $MnPS_3$, $FePS_3$, $CoPS_3$, $NiPS_3$, and $ZnPS_3$ thiophosphates whose bulk structure had been explored in past experiments [24,26–41,51–54]. We have optimized MPX_3 lattice structures using the unit cell shown in Fig. 1 for single layers and assuming ABC stacking for bulk. Given this framework, structures are characterized by the value of the in-plane lattice constant a, the (P-P) distance between the phosphorous atoms, the (M-M) distance between metal atoms, and the (P-X) distance between phosphorous atoms and chalcogen atoms. The variation in the magnitude of these bond lengths as a function of the metal and chalcogen atom species, and magnetic configuration, is illustrated in Fig. 2, and summarized numerically in Table II of the Supplemental Material [61]. Results are presented for all metastable magnetic states. The structures have a simple dependence on chalcogen atom size, with larger in-plane lattice constants and monolayer thicknesses (P-P distances) for larger chalcogens. However, the dependence of the structure on the metal atom atomic number is not straightforward. Experiments in the bulk MPS_3 observed a close correlation between the radius of the metal cation and the P-P distance of the thiophosphate bipyramid [24]. The nonmonotonic variation of the metal cation radius with respect to atomic number is reflected in the P-P distance trend. However, our calculations show that bond lengths correlate more strongly with magnetic state than with metal atomic number.

P-P distances range between 2.15–2.3 Å, while M-M bond lengths vary by about 5%. The M-M bond lengths within a hexagon can be unequal, distorting the hexagonal lattice arrangement of the metal atoms, as illustrated in Fig. S1 in the Supplemental Material [61]. In general, ferromagnetic
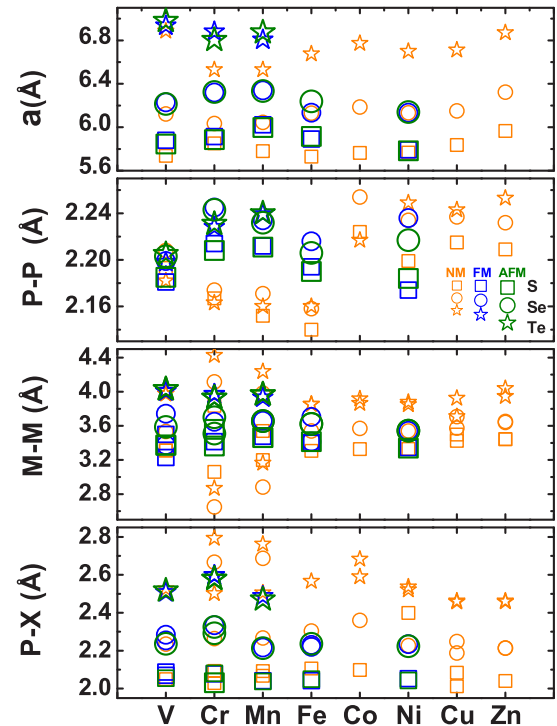

FIG. 2. Summary of key structure metrics (in-plane lattice constant, P-P bond length, M-M bond length, and P-X bond length) in single-layer MPX_3 compounds. Bond lengths increase with the size of the chalcogen atom (S: square; Se: circle; Te: star) and a strong systematic dependence on whether the magnetic state is NM (nonmagnetic: orange), FM (ferromagnetic: blue), or antiferromagnetic (AFM: green), but have a more complex nonmonotonic dependence on the metal atomic number,

states have the largest lattice constants, and antiferromagnets have intermediate lattice constants. The fact that the structural properties of these crystals are correlated with their magnetic configurations suggests the possibility of controlling magnetic properties by straining the lattice, as we will discuss in more detail in a later section.

The comparison between lattice parameters calculated with GGA+D2 and the experimental bulk structure is summarized in Table I. The comparison of the GGA and LDA lattice parameters in Table I of the Supplemental Material [61] indicates important discrepancies between the GGA and LDA, and is consistent with the tendency of the LDA to overbind covalent bonds. The stronger LDA bonds lead to a global reduction of lattice constant and to a stronger distortion of the metal honeycombs. Within the LDA, we find optimized lattice parameters that are (2–5%) shorter than in bulk experiments. The GGA agreement is good (0.5–1.6%) for $MnPS_3$, $FePS_3$, $CoPS_3$, $NiPS_3$, and $ZnPS_3$.

B. Magnetic properties

Experimental studies of the magnetic properties of bulk Mn, Fe, Co, and Ni thiophosphates have found antiferromagnetic ground states with Néel temperatures ranging between ~82–155 K [24,25]. Here we find that magnetism persists

TABLE I. Comparison between experimental and theoretical bulk lattice parameters, and theoretical two-dimensional lattice parameters, for transition-metal phosphorous trichalcogenide MPX_3 compounds. These results were obtained using GGA+D2 and are expressed in Å. a is the in-plane lattice constant and c' is the layer thickness, i.e., it is the distance between the planes containing the three chalcogen atoms in a single MPX_3 layer. The values in parentheses below the bulk c'(Å) values are the interlayer distances, i.e., the vertical distances between the top X atom of one layer and the bottom X atom of an adjacent layer.

MPX_3	X	NM		FM		AFM	
		a (Å)	c' (Å)	a (Å)	c' (Å)	a (Å)	c' (Å)
	S	5.737	3.142	5.880	3.166	5.846	3.170
	S (bulk)	5.742	3.280	5.918	3.273	5.845	3.294
			(3.252)		(3.314)		(3.381)
	S (Expt)						
VPX_3	Se	6.123	3.266	6.230	3.204	6.214	3.318
	Te	6.885	3.328	6.935	3.418	6.980	3.431
	S	5.851	3.071	5.914	3.032	5.885	3.336
	S (bulk)	5.862	3.116	5.913	3.185	5.934	3.301
			(3.154)		(3.285)		(3.383)
	S (Expt)						
CrPX_3	Se	6.035	3.367	6.320	3.100	6.325	3.235
	Te	6.530	3.672	6.880	3.330	6.804	3.388
	S	5.780	2.952	6.023	3.256	5.997	3.246
	S (bulk)	5.787	2.875	6.018	3.125	5.993	3.268
			(3.127)		(3.270)		(3.264)
	S (Expt)					6.076	
MnPX_3	Se	6.045	3.182	6.340	3.416	6.334	3.402
	Te	6.530	3.444	6.805	3.550	6.874	3.535
	S	5.730	2.808	5.891	3.150	5.958	3.180
	S (bulk)	5.736	2.969	5.874	3.313	5.921	4.368
			(3.235)		(3.603)		(4.121)
	S (Expt)					5.934	
FePX_3	Se	6.130	2.911	6.134	3.347	6.239	3.214
	Te	6.676	3.038				
	S	5.763	2.790				
	S (bulk)	5.784	4.250				
			(4.929)				
	S (Expt)	5.901					
CoPX_3	Se	6.186	2.850				
	Te	6.772	3.057				
	S	5.766	2.974	5.792	3.064	5.783	3.042
	S (bulk)	5.763	2.995	5.789	3.062	5.779	3052
			(3.207)		(3.205)		(3.230)
	S (Expt)					5.813	
NiPX_3	Se	6.132	3.086	6.134	3.100	6.140	3.142
	Te	6.700	3.208				
	S	5.837	3.439				
	S (bulk)	5.843	3.903				
			(3.693)				
	S (Expt)						
CuPX_3	Se	6.151	3.532				
	Te	6.711	3.617				

TABLE I. (*Continued.*)

MPX_3	X	NM		FM		AFM	
		a (Å)	c' (Å)	a (Å)	c' (Å)	a (Å)	c' (Å)
	S	5.966	3.230				
	S (bulk)	5.973	3.025				
			(3.716)				
	S (Expt)	5.971					
ZnPX_3	Se	6.323	3.379				
	Te	6.871	3.597				

in single-layer MPX_3 compounds. The magnetic moments develop mainly at the localized metal atom sites, except for a noticeable spin polarization that develops on the phosphorous and sulfur atom sites in the ferromagnetic configuration.

The late $3d$ transition elements Cr, Mn, Fe, Co, and Ni stand out in the periodic table as elements that tend to order magnetically. The bonding arrangements of particular compounds can, however, enhance or suppress magnetism. In 2D MPX_3 crystals, transition-metal atoms are contained
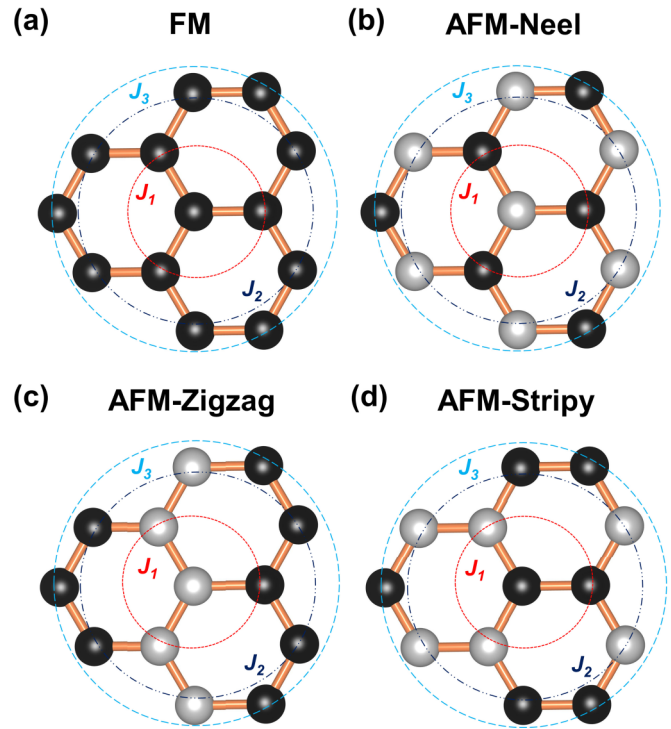

FIG. 3. Top view of different magnetic ordering arrangements: (a) ferromagnetic, (b) Néel antiferromagnetic, (c) zigzag antiferromagnetic, and (d) stripy antiferromagnetic. In MPX_3 compounds, the magnetic moments reside primarily on the metal atoms which have a honeycomb structure in each layer. The black and white spheres represent up and down spins, respectively. The red circles identify nearest neighbors (NN) of the central metal site, the navy blue circles (dash-dotted) identify the second-nearest neighbors, and the light blue circles identify the third-nearest neighbors. The magnetic energy landscape can be approximated by assigning Heisenberg coupling constants J_1, J_2, and J_3 to metal atom pairs with these three separations.

TABLE II. Total energy relative to that of the lowest-energy magnetic configuration calculated using the GGA+D2 approximation for the ferromagnetic (FM), antiferromagnetic (AFM), and nonmagnetic (NM) states of single-layer transition-metal phosphorous trichalcogenides MPX_3. The absence of an entry for a magnetic configuration means that the corresponding state is not metastable. Energies are expressed in terms of meV/unit cell. Our first-principles calculations suggest stable magnetic phases for V, Cr, Mn, Fe, and Ni metal compounds. The rectangular supercells and structural triangular unit cells used in these calculations are illustrated in Fig. 1. The smaller triangular unit cell is used to compare the NM, FM, and Neel AFM phases and the larger rectangular unit cell is needed when we also compare with the total energies of zAFM and sAFM phases. The work functions are in eV units for the smaller triangular unit cell.

MPX_3	X	Rectangular					Triangular			Work function (eV)		
		NM	FM	AFM	zAFM	sAFM	NM	FM	AFM	NM	FM	AFM
	S	1142.8	643.2	0.0	246.9	132.7	1083.8	695.8	0.0	3.56	3.26	3.42
VPX_3	Se	906.9	275.8	0.0	164.6	87.78	1348.1	458.8	0.0	2.82	3.57	3.58
	Te	0.0	399.3	323.9	371.4	327.9	1296.5	183.1	0.0	3.08	3.88	3.85
	S	1454.5	0.0	91.65	30.62	63.23	1182.5	0.0	73.68	3.40	3.07	3.62
$CrPX_3$	Se	1514.6	0.0	146.1	57.06	522.7	1293.7	0.0	315.4	3.98	3.52	3.65
	Te	1373.4	0.0	242.9	81.31	12.06	1482.6	0.0	264.2	3.74	3.55	3.41
	S	1576.2	186.3	0.0	60.68	74.59	1964.1	205.4	0.0	3.74	4.41	3.98
$MnPX_3$	Se	1356.6	156.7	0.0	48.96	68.98	1417.3	166.4	0.0	3.98	4.07	3.91
	Te	0.0					840.0	12.44	0.0	3.68	3.66	3.77
	S	141.5	286.8	115.8	0.0	289.0	44.87	0.0	308.3	3.41	4.13	4.23
$FePX_3$	Se	0.0					0.0	165.0	324.5	3.93	3.73	3.86
	Te	0.0					0.0			3.32		
	S	0.0					0.0			3.84		
$CoPX_3$	Se	0.0					0.0			4.33		
	Te	0.0					0.0			3.50		
	S	507.5	276.7	64.16	0.0	343.5	425.1	213.4	0.0	4.63	4.91	5.08
$NiPX_3$	Se	324.8	196.2	0.0	383.2	278.2	168.0	158.8	0.0	4.79	4.54	4.44
	Te	0.0					0.0			2.58		
	S	0.0					0.0			4.96		
$CuPX_3$	Se	0.0					0.0			5.15		
	Te	0.0					0.0			2.96		
	S	0.0					0.0			3.97		
$ZnPX_3$	Se	0.0					0.0			4.47		
	Te	0.0					0.0			1.11		

within phosphorous trichalcogenide bipyramidal cages, and have weak direct hybridization with other transition-metal atoms. The exchange interactions between the metal atoms are therefore mainly mediated by indirect exchange through the intermediate chalcogen and P atoms. Magnetic interactions can be extracted from *ab initio* electronic structure calculations by comparing the ground-state energies of different magnetic configurations. We compare the energies of antiferromagnetic, ferromagnetic, and nonmagnetic states in V-, Cr-, Mn-, Fe-, and Ni-based compounds in Table II, where we find that the AFM phase is normally favored over the FM phase.

Because our calculations show that the magnetic moments are concentrated at the metal atoms sites, we can characterize the magnetic properties of 2D MPX_3 compounds by mapping the energy landscape to an effective classical spin Hamiltonian on a honeycomb lattice,

$$H = \sum_{\langle ij \rangle} J_{ij} \, \vec{S}_i \cdot \vec{S}_j = \frac{1}{2} \sum_{i \neq j} J_{ij} \, \vec{S}_i \cdot \vec{S}_j, \qquad (1)$$

where $\vec{S}_i$ is the total spin magnetic moment of the atomic site i, J_{ij} are the exchange coupling parameters between two

local spins, and the prefactor 1/2 accounts for the double counting. The estimated magnetic anisotropy energies that we obtained from noncollinear magnetization calculations are of the order of $\sim 160 \, \mu$eV per formula unit for the FM compounds $CrPS_3$ and $CrPSe_3$, and of the order of $\sim 1000 \, \mu$eV per formula unit for the AFM compounds $MnPS_3$ and $MnPSe_3$ with magnetization favored perpendicular to the plane. For this reason, in making the T_c estimates that we describe below, we take the Ising limit of this spin Hamiltonian. By evaluating the three independent energy differences between the four magnetic configurations [18,24,62] illustrated in Fig. 3, i.e., ferromagnetic (FM), Néel (AFM), zigzag AFM (zAFM), and stripy AFM (sAFM), and assuming that the magnetic interactions are short range, we can extract the nearest-neighbor (J_1), second-nearest-neighbor (J_2), and third-nearest-neighbor (J_3) coupling constants [18]:

$$E_{\mathrm{FM}} - E_{\mathrm{AFM}} = 3(J_1 + J_3) \, \vec{S}_A \cdot \vec{S}_B, \qquad (2)$$

$$E_{\mathrm{zAFM}} - E_{\mathrm{sAFM}} = (J_1 - 3J_3) \, \vec{S}_A \cdot \vec{S}_B, \qquad (3)$$

$$E_{\mathrm{FM}} + E_{\mathrm{AFM}} - E_{\mathrm{zAFM}} - E_{\mathrm{sAFM}} = 8J_2 \, \vec{S}_A \cdot \vec{S}_A, \qquad (4)$$

where $\vec{S}_X$ is the average spin magnetic moment on the honeycomb sublattice X. The total energies of the zAFM and sAFM magnetic configurations, which must be calculated using a rectangular supercell, usually have higher energies than the average of the AFM solutions and FM solutions. The larger rectangular unit cell required for describing more complex zAFM and sAFM spin configurations imposes certain symmetries that restrict the relaxation of the lattices when compared to the triangular unit cell. For the case of FePS$_3$, however, the zAFM has the lowest energy. The average magnetic moments S at each lattice site obtained within the GGA+D2 and GGA+D2+U are listed in Table III.

Single-layer magnetic ordering temperatures T_c were estimated by running Monte Carlo simulations of the three-coupling-constant effective models using the Metropolis algorithm in lattice sizes up to $N = 32 \times 64$ with periodic boundary conditions [63–65], and verified against calculations performed using the Wang-Landau Monte Carlo sampling algorithm in smaller $N = 8 \times 16$ lattices [66]. We calculated the heat capacity $C = k\beta^2(\langle E^2 \rangle - \langle E \rangle^2)$ as a function of temperature and identified its diverging point as the Neel and Curie temperatures. See the Supplemental Material [61] for the plot of the representative results for the temperature-dependent heat capacity.

The calculated average values of the magnetic moments in the AFM configuration vary widely, assuming the values 2.01, 3.14, 4.16, 3.2, 0.8, and 1.14 μ_B for V-, Cr-, Mn-, Fe-, Co-, and Ni-based sulfides (see Table III). The magnitudes of the magnetic moments at the metal atoms generally have relatively small differences between different magnetic configurations, between $\sim$3–10%, while larger variations are found in CoPS$_3$ and NiPSe$_3$. Within the GGA+D2 approximation, we find that the magnetic moments in 2D MPX_3 develop almost entirely at the metal atom sites. In comparison, the phosphorous and chalcogens in the bulk structure do acquire a small spin

polarization that can be attributed to interlayer coupling. The use of on-site U introduces a small spin-polarization enhancement at nonmetal atom sites.

C. Band structure and density of states

Understanding the electronic properties of 2D MPX_3 layers is an essential stepping stone on the path toward possible integration in nanodevices. For spintronic applications of magnetic 2D materials, which seek to couple charge and spin degrees of freedom, it is desirable to understand how the electronic structure depends on the type of magnetic order. The spin-resolved band structures of the lowest-energy spin configuration, calculated within the GGA+D2 approximation, are presented in Fig. 4, the associated densities of states are presented in Fig. 5, and the projected partial density of states (PDOS) results for various MPX_3 compounds presented in Fig. 6. Single-layer MPX_3 with $M =$ V, Cr, Mn, Fe, Co, Ni, Cu, and Zn transition-metal atoms and $X =$ S, Se, and Te chalcogen atoms are considered. Band structures for higher-energy spin configurations are included in the Supplemental Material [61].

We find that AFMs are almost always gapped semiconductors, FM states are metallic, and NM phases can be either semiconducting or metallic. It follows that the MPX_3 class of materials includes almost all of the behaviors being studied in current spintronics research, including importantly both anti-ferromagnets and ferromagnets and both metals and insulators.

The AFM band structures for V- and Mn-based compounds in Fig. 4 show semiconductor behavior and reveal conduction-band edges that are near the K points, whereas the valence-band edges are between Γ and K. These valence bands near the Fermi energy are energetically separated from deeper-lying valence bands. We notice from the density of states plot in Fig. 5 that there is strong sensitivity of the electronic structure to the choice of electron-electron interaction model, both for

TABLE III. Magnetic moments in Bohr magneton μ_B per metal atom for bulk and single-layer magnetic MPX_3 structures, the three nearest-neighbor exchange coupling strengths J_i in meV implied by the Heisenberg model mapping, and Monte Carlo estimates of the single-layer critical temperatures based on the Ising limit of the classical spin model. The critical temperature is identified with the maximum in the derivative of magnetization with respect to temperature. The Ising limit estimate is motivated by the strong perpendicular anisotropy of these materials. The *ab initio* calculations were performed within GGA+D2, as well as GGA+D2+U using a constant site repulsion at the metal atoms of $U = 4$ eV. The magnetization is calculated as the difference between up and down local spin-resolved charge densities as implemented in QUANTUM ESPRESSO.

| MPX_3	X	Bulk		GGA+D2								GGA+D2 + U							
		FM	AFM	FM	AFM	zAFM	sAFM	J_1	J_2	J_3	T_c	FM	AFM	zAFM	sAFM	J_1	J_2	J_3	T_c
VPX_3	S	2.03	2.00	1.92	2.01	1.68	1.76	24.5	4.26	3.24	1100	2.96	2.93	2.95	2.93	3.93	0.147	0.143	570
	Se			2.02	2.13	1.77	2.14	10.2	0.340	0.437	760	2.56	2.99	3.01	2.98	2.81	0.132	0.170	400
	Te			2.22	2.16	2.06	2.19	9.63	−3.59	−7.07	570	3.10	3.08	3.13	3.08	5.10	−1.68	−3.51	560
CrPX_3	S	2.83	3.07	2.85	3.14	2.37	2.34	−1.73	−0.015	0.029	280	3.94	4.03	3.93	4.11	1.34	−0.064	−0.490	130
	Se			2.77	2.83	2.45	2.38	−9.82	−3.49	6.62	1080	4.14	4.03	4.04	4.11	0.608	−0.254	−3.05	250
	Te			2.92	2.88	2.82	2.48	−4.89	0.006	−0.087	750	4.25	4.17	4.17	4.21	0.849	0.333	−2.10	900
MnPX_3	S	4.24	4.15	4.26	4.16	3.82	3.83	1.21	0.180	0.536	500	4.56	4.54	4.54	4.55	0.369	0.0284	0.152	200
	Se			4.25	4.20	4.24	3.82	0.958	0.136	0.506	450	4.56	4.54	4.55	4.56	0.231	0.021	0.141	150
FePX_3	S	3.32	3.14	3.33	3.20	3.24	2.48	−1.59	−0.179	3.00	690	3.48	3.46	3.48	3.47	0.575	0.140	0.69	260
NiPX_3	S	1.25	1.13	1.26	1.14	1.12	1.20	−11.3	−0.115	36.0	1110	1.21	1.17	1.22	1.19	−4.11	1.95	17.4	560
	Se			0.54	0.94	0.12	0.99	127	−82.3	−67.6	2580	1.14	1.08	1.22	1.14	−3.11	1.04	18.2	510
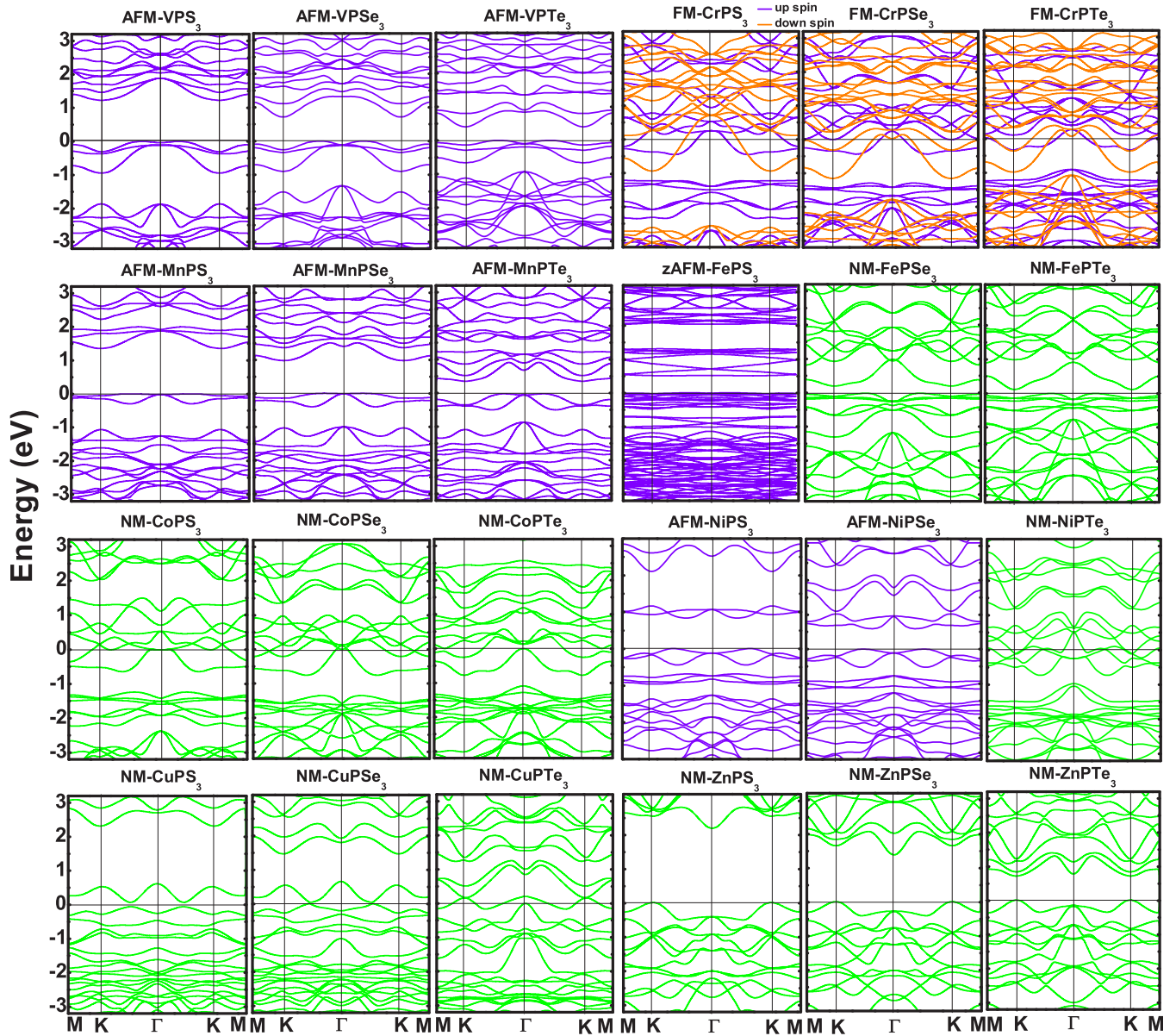
FIG. 4. GGA+D2 band structures for single-layer MPX_3 compounds in their lowest-energy magnetic configuration for $M =$ V, Cr, Mn, Fe, Co, Ni, Cu, and Zn transition-metal atoms and $X =$ S, Se, Te chalcogen atoms. The plotted band structures were calculated using the triangular structural unit cell, except for the case of FePS$_3$, which is predicted to have a larger periodicity zAFM (see text) magnetic structure that has a triangular unit cell with a doubled lattice constant. The bands are violet for AFM configurations, violet and orange for the up and down split spin bands in the FM configurations, and green for the NM phases. We note that the AFM phases have semiconducting band gaps and that the FM phases are metallic, while the nonmagnetic phases can be either metallic or semiconducting. An overall reduction of the band gaps is observed when we use heavier chalcogen atoms, in keeping with the reduction of the covalent bond energy in larger shell orbitals.

the HSE+D2 approximation containing nonlocal exchange and for on-site repulsion enhancement introduced through a Hubbard U parameter. The analysis of the orbital projected partial density of states in Fig. 6 for the AFM compounds reveals that the conduction-band edges have an important contribution from the s and p orbitals of the P atom, while for the valence-band edges, the chalcogen atom orbitals have an importance presence. Other atoms do contribute near the band edges, e.g., for the V-based compounds, the d orbitals are an important fraction of the valence-band edge, while for the Mn-based compounds, they lie at deeper energies. We can thus expect that surface functionalization and variations in

the carrier density at the surface chalcogens will have a more immediate impact in the valence bands than the conduction bands. The AFM compounds containing Fe and Ni result in nonmagnetic solutions when heavier chalcogen atoms are used within our GGA+D2 calculation. The case of FePS$_3$ has, as the lowest-energy configuration, the zigzag AFM phase.

For MPX_3 compounds, the FM configurations are metallic as a general rule. Within our GGA+D2 approximation, only the Cr-based chalcogenophosphates have FM ground states, while they favor the AFM phase when the on-site U is added; see the Supplemental Material [61] for GGA+D2+U results. We find that the FM configurations are often metastable local
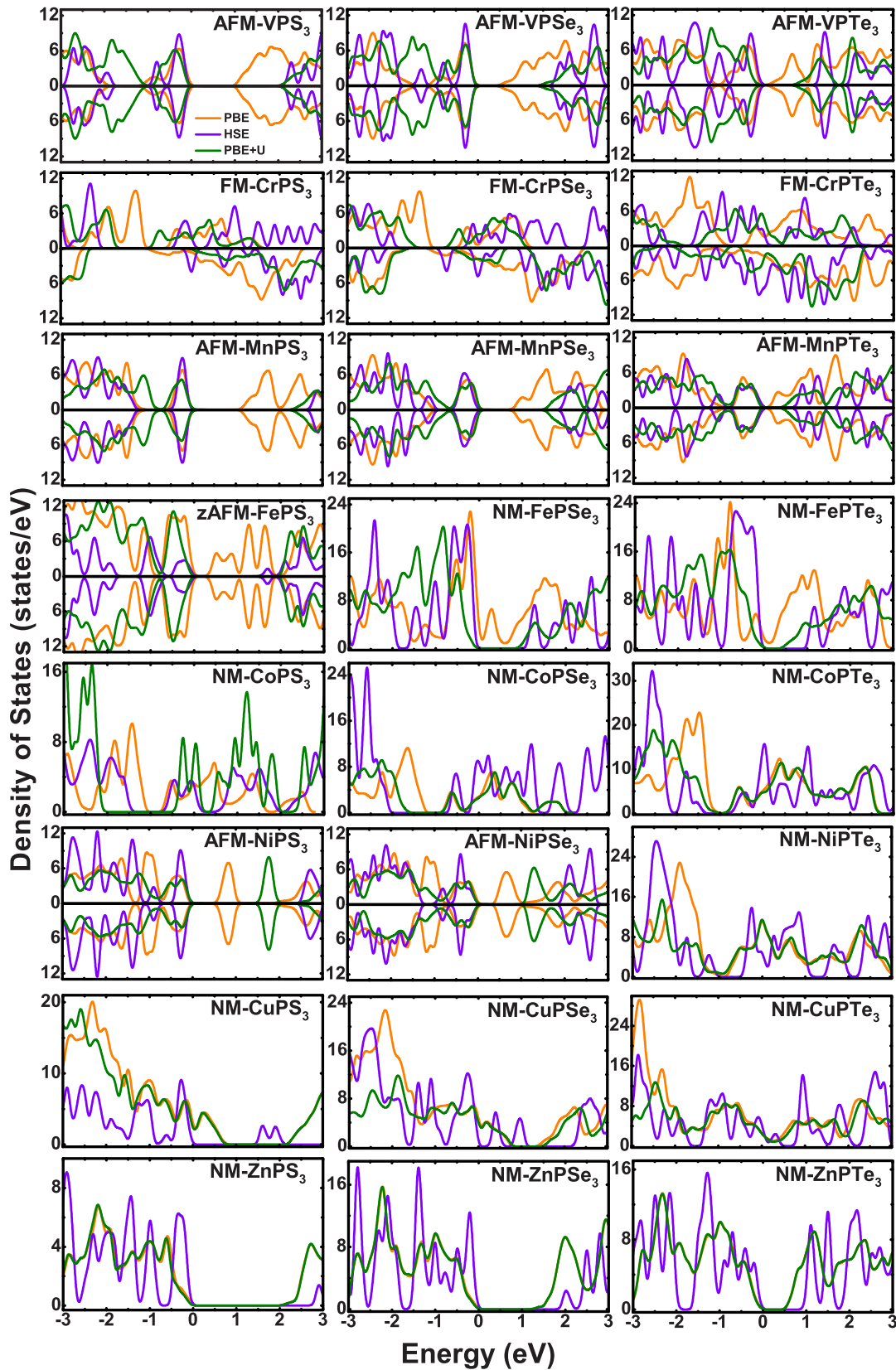
FIG. 5. Total density of states (DOS) for the magnetic ground states in Fig. 4, calculated using three different exchange-correlation energy functional calculations: GGA+D2, HSE+D2, and GGA+D2+U. We have placed the valence-band edge at $E = 0$. Overall band-gap enhancements are found for the semiconducting phases when additional electron-electron interactions are approximated as nonlocal exchange corrections in HSE+D2 and as on-site repulsion corrections in GGA+U. Both HSE and GGA+U enhance the band gaps. Other features in the DOS plots also depend on the DFT exchange-correlation functional approximation.
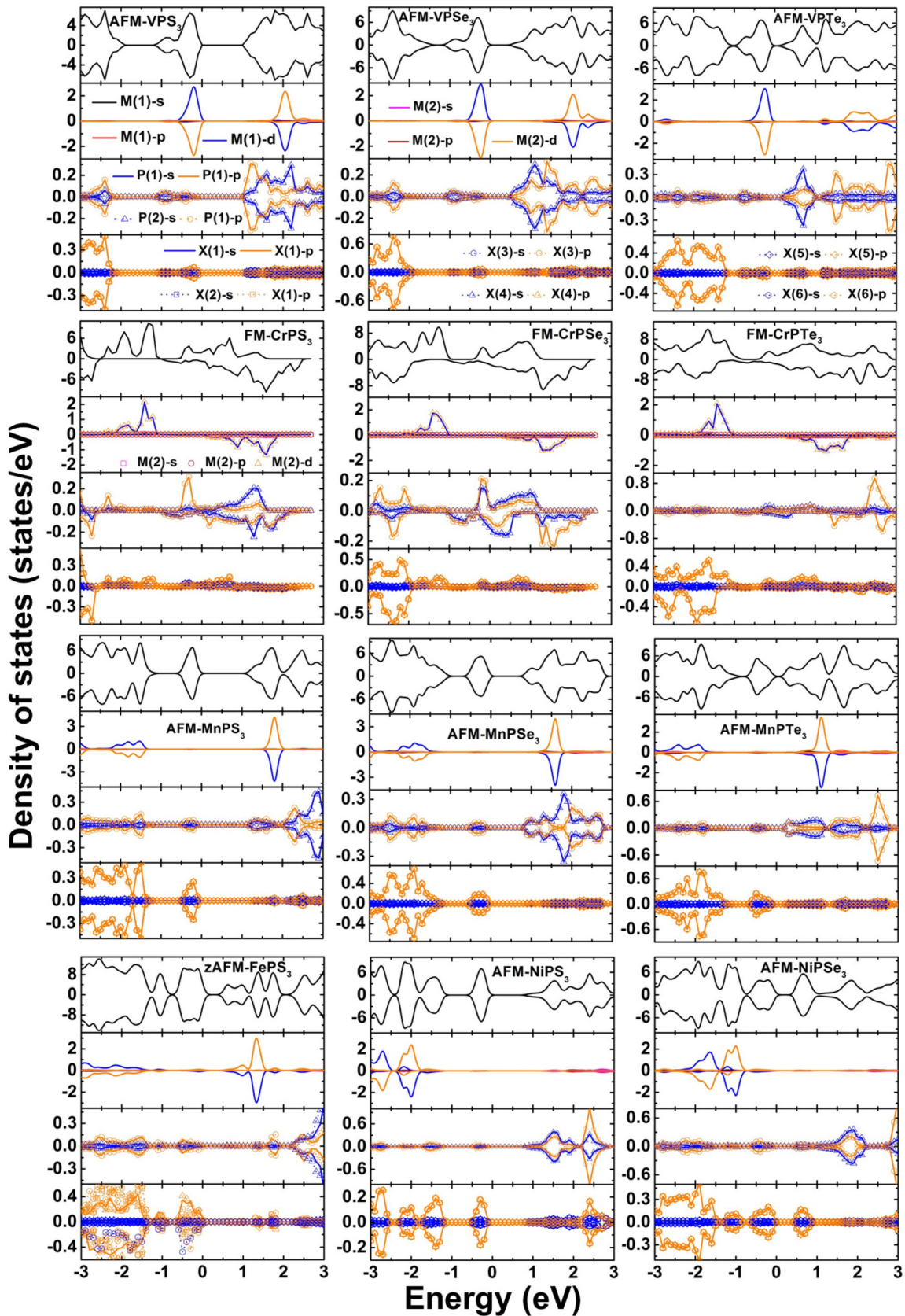
FIG. 6. Orbitally projected partial density of states (PDOS) calculated for self-consistently converged ground-state magnetic configurations. The zero of energy is chosen at the valence-band edge. From the PDOS of the various MPX_3 compounds, we observe that the orbital content of the valence- and conduction-band edges vary widely. For the compounds showing carrier-density-dependent magnetism, the states closest to the Fermi energy generally have an important contribution from the p orbitals of the chalcogen and P atoms.

TABLE IV. Band gaps of MPX_3 compounds predicted to have antiferromagnetic semiconductor ground states. The band gaps are listed in eV energy units and have values that depend substantially on the DFT exchange-correlation approximation employed. Values are listed for GGA+D2, HSE+D2 hybrid functional, and GGA+D2+U approximations. The magnitude of U was chosen to maximize the band gap. As expected, the HSE+D2 functional yields the largest band gaps.

	X	GGA+D2	HSE+D2	GGA+D2+U
	S	1.23	2.50	2.32 ($U = 3.25$)
VPX_3	Se	0.73	2.10	1.67 ($U = 3.25$)
	Te	0.41	1.57	1.00 ($U = 3.25$)
	S	1.36	3.05	2.34 ($U = 5.0$)
MnPX_3	Se	0.98	2.24	1.70 ($U = 5.0$)
	Te	0.38	1.06	0.69 ($U = 5.0$)
	S	0.57	2.07	2.26 ($U = 5.3$)
FePX_3	Se	0.20	1.48	1.19 ($U = 5.3$)
	Te	0.13	1.35	0.59 ($U = 5.3$)
	S	0.84	2.83	1.74 ($U = 6.45$)
NiPX_3	Se	0.59	2.22	1.31 ($U = 6.45$)
	Te		0.27	
	S	0.01	1.76	0.08 ($U = 1.0$)
CuPX_3	Se		0.56	
	S	2.19	3.11	2.23 ($U = 5.4$)
ZnPX_3	Se	1.38	2.19	1.41 ($U = 5.4$)
	Te	0.73	1.26	0.74 ($U = 5.4$)

minima solutions in MPX_3 compounds whose lowest-energy solutions are AFM. The FM configurations are found in the metallic phase at charge neutrality and give rise to half-metallic solutions for MnPS$_3$ and NiPS$_3$. The half metallicity could be achieved also in MnPSe$_3$ when carrier doped away from neutrality. For the MnPS$_3$ and MnPSe$_3$ compounds, we can observe a distinct population of the carriers for the hole and electron sides where doping populates orbitals located at the chalcogen and P atoms, respectively.

The electronic properties of NM configurations are also presented in Figs. 4 and 5. The NM layers could be potentially interesting if magnetic phases could be induced by forming vertical heterojunctions with magnetic materials. Unexpectedly, one typically magnetic element (Co) turns out to be nonmagnetic in MPX_3 compounds according to our GGA+D2-based calculations. As shown in Fig. 4, the band structure of these nonmagnetic materials can be metallic (Co-, Ni-, and Cu-based compounds), semiconducting (Fe), or a wide gap insulator (Zn).

We now turn our attention to the magnitude of the band gaps of the semiconducting and insulating 2D MPX_3 chalcogenophosphates calculated within the GGA approximation, and using other approximations that partially account for Coulomb correlation through nonlocal exchange or a Hubbard U, as shown in Table IV. These gaps are consistently larger when calculated using the hybrid HSE+D2 approximation, which includes nonlocal exchange in the energy functional. A smaller gap enhancement is obtained using a +U interaction correction. Band gaps are gradually reduced when S is replaced by heavier chalcogen atoms.

The corresponding density of states (DOS), plotted in Fig. 5, shows the strong influence on the ground-state electronic structure when Coulomb correlations are included. Note in particular the impact of the nonlocal Coulomb exchange included in the HSE approximation. This suggests that the physics of MPX_3 compounds can be dominated by correlation effects and modeling will be most successful when we rely on effective models that feed from experimental input or high-level *ab initio* calculations.

The orbital content of the valence- and conduction-band edges that are most relevant for studies of carrier-density-dependent magnetic properties can be extracted from the orbital projected partial density of states (PDOS) results for various MPX_3 compounds presented in Fig. 6. Depending on the specific composition and on the magnetic configuration of the material under consideration, the valence- and conduction-band edge orbitals can be dominated by metal, phosphorous, or chalcogen atoms. A detailed study of the influence of the Coulomb interaction model on the localization properties of the wave functions and their influence on the exchange coupling in MPX_3 compounds will be presented elsewhere.

IV. TUNABILITY OF MAGNETIC PROPERTIES

Two-dimensional magnetic materials are of interest primarily because of the prospect that their properties might be more effectively altered by tuning parameters that are available *in situ*. Two potentially important control knobs that can be exploited experimentally in two-dimensional-material-based nanodevices are carrier density and strain. The dependence of magnetic properties on carrier density is particularly interesting because it provides a convenient route for electrical manipulation of magnetic properties. In this section, we explore the possibility of tailoring the electronic and magnetic properties of MPX_3 ultrathin layers by adjusting carrier density or by subjecting the MPX_3 layers to external strains.

A. Field-effect modification of magnetic properties

The goal of modifying the magnetic properties of a material simply by applying a gate voltage is a holy grail in magnetoelectronics because it could allow magnetically stored information to be written at negligible energy cost. Electric field control of magnetic order has been demonstrated in a number of materials. In ferromagnetic semiconductors, the mechanism is carrier-density variation in thin films, which leads to a modification of the magnetic exchange interaction and magnetic anisotropy. In thin films of ferromagnetic metals, gate voltages can vary the Fermi level position at the interface, which governs the magnetic anisotropy of the metal [67–69].

We leave to future work a complete microscopic analysis of the response of a MPX_3 layer, acting as one electrode of a capacitor, to a gate voltage. Here we capture the most important response by simply examining the dependence of magnetic properties on carrier density. In doing so, we neglect the possible role of charge polarization within a MPX_3 layer. Figure 7 summarizes the theoretically predicted trends in competition between AFM and FM states in 2D MPX_3 compounds with $M =$ V, Cr, Mn, Fe, Ni and $X =$ S, Se, Te. We find that when the magnetic ground state is AFM ($M =$ V, Mn,
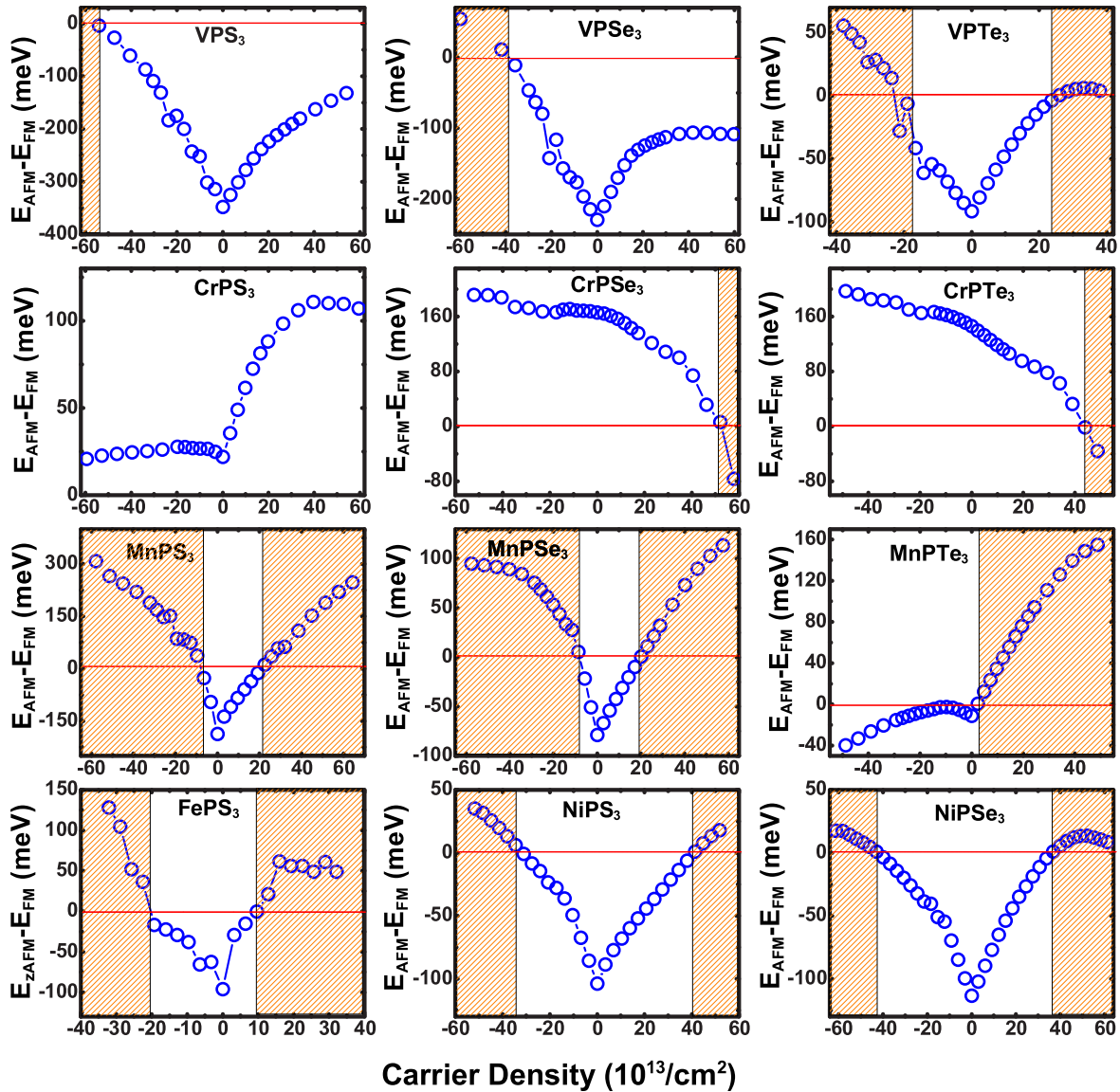
FIG. 7. Carrier-density-dependent total-energy differences per MPX_3 formula unit between the AFM and FM states of V-, Cr-, Mn-, Fe-, and Ni-based single-layer trichalcogenides. The prominent cusps in these curves appear because the antiferromagnetic state has a band gap, whereas the ferromagnetic state does not have a band gap. The AFM ground states favored near charge neutrality can be switched to FM states at accessible carrier densities in V-, Mn-, Ni-, and Fe-based compounds. For $CrPX_3$ with $X = $ Se or Te, it is possible to switch from a FM to an AFM state at finite n doping. Carrier densities of up to a few $\sim 10^{14}$ electrons per cm^2 should, in principle, be accessible through ionic liquid or gel gating. A carrier density of 0.1 electrons per MPX_3 formula unit corresponds to $\sim 6 \times 10^{13}$ electrons per cm^2 when the lattice constant is ~ 6 Å.

Ni, Fe), transitions to FM states are driven by sufficiently large electron or hole carrier densities. The origin of this trend is easy to understand. Because the FM state is gapless, the energy changes associated with adding one electron and removing one electron are identical. In the gapped AFM states, they differ by the energy gap E_{gap}. It follows that the energy difference per area unit between antiferromagnetic and ferromagnetic states, $\delta E \equiv E_{\text{AFM}} - E_{\text{FM}}$, is given at low carrier densities by

$$\delta E(n) = \delta E_0 + (E_{\text{gap}}/2 + \delta \mu)\, n,$$

$$\delta E(p) = \delta E_0 + (E_{\text{gap}}/2 - \delta \mu)\, p, \qquad (5)$$

where n is the carrier density of n-type samples, p is the carrier density of p-type samples, δE_0 is the energy difference per

area unit between antiferromagnetic and ferromagnetic states in neutral MPX_3 sheets, and $\delta \mu$ is the difference between the midgap energy of the antiferromagnetic semiconductors and the chemical potential of the ferromagnetic metals. Introducing n carriers is most effective in driving a transition from antiferromagnetic to ferromagnetic states when $\delta \mu$ is positive, whereas introducing p carriers is most effective when $\delta \mu$ is negative. By comparing with Fig. 7, we conclude that $\delta \mu$ is small in most cases, but large and negative in MnPS$_3$ and MnPSe$_3$. Because the energy difference per formula unit between ferro- and antiferromagnetic states is much smaller than the energy gap, a transition between antiferromagnetic and ferromagnetic states can be driven by carrier-density changes per formula unit that are much smaller than one—
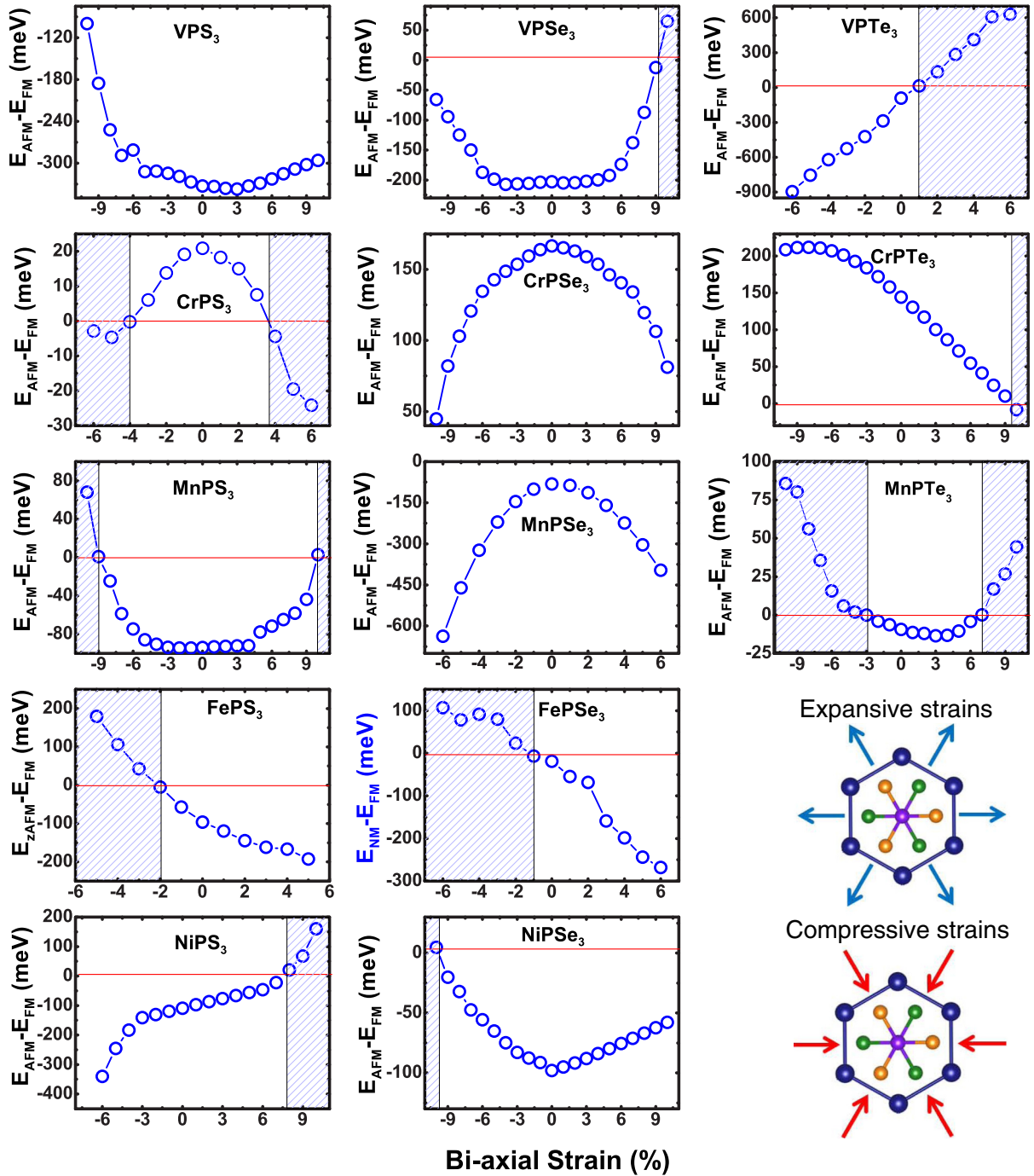
FIG. 8. Influence of in-plane strain on the magnetic configurations of selected MPX_3 compounds. Magnetic phase transitions are introduced by in-plane biaxial compressive and expansive strains for several magnetic MPX_3 compounds at zero carrier density. Particularly sensitive strain dependence is seen for FePS$_3$, FePSe$_3$, and VPTe$_3$, where small strains of the order of 1% of the lattice constant can switch the magnetic phases.

especially so when $\delta\mu$ plays a favorable role. In particular, we see in Fig. 7 that a transition between ferromagnetic and antiferromagnetic states is predicted in MnPS$_3$ and MnPSe$_3$ at hole carrier densities that are $\sim 10^{14}$ cm^{-2}, which corresponds to about ~ 0.16 electrons per formula unit. Density changes of this magnitude can be achieved by ionic liquid or gel gating. Since this size of carrier density is sufficient to completely change the character of the magnetic order, we can expect substantial changes in magnetic energy landscapes at much

smaller carrier densities. Transitions between ferromagnetic and antiferromagnetic states are predicted in most MPX_3 compounds. Our calculations show that the FM solution is the preferred stable magnetic configuration in almost all cases when the system is subject to large electron or hole densities in the range above a few times $\pm 10^{14}$ cm^{-2}. The DOS and PDOS shown in Figs. 5 and 6 in the main text and in Figs. 5–10 in the Supplemental Material [61] may suggest that a Stoner ferromagnetic instability is at play when the peaks near

the band edges are sufficiently prominent. Our calculations therefore motivate efforts to find materials which can be used to establish good electrical contacts to MPX_3 compounds, and in particular to the valence bands of MnPS$_3$ and MnPSe$_3$. For the Cr-based compounds, whose behavior is different, the ground states at zero carrier density are FM and we find that a transition to an AFM state can occur for n-doped systems.

B. Strain-tunable magnetic properties

The membranelike flexibility of ultrathin 2D materials makes them suitable platforms for tailoring the electronic structure properties by means of strains. Representative examples of the effects of strains in 2D material properties that have been discussed in the recent literature include the observation of Landau-level-like density of states near high-curvature graphene bubbles [70], or the commensuration Moire strains that open up a band gap at the primary Dirac point in graphene on hexagonal boron nitride for sufficiently long Moire patterns [71–73]. The sensitive variation of the different M-M, P-P, and M-X bond lengths as a function of magnetic configuration that we presented in Sec. III suggests that strains can be used as switches to trigger magnetic phase transitions or alter the stability of the magnetic phases by modifying the total-energy difference with respect to the nonmagnetic phases. Here we have carried out calculations of the total energies for different magnetic phases to explore the influence of expansive or compressive in-plane biaxial and uniaxial strains and the effects of external pressure along the out-of-plane axis in 2D MPX_3 materials, see Fig. 8. The compressive and expansive biaxial strains have been modeled through uniform scaling of the rectangular unit cell in Fig. 1 and likewise the uniaxial strains are modeled by scaling the unit cell either in the zigzag or armchair directions. We notice that generally the effects of uniform biaxial versus uniaxial strains introduce modifications in the magnetic phase energy difference total energies that are qualitatively similar for the compressive or expansive strains, and that the effects are stronger for biaxial strains when compared to uniaxial strains which do not show a noticeable difference between the zigzag or armchair directions. Pressure strains along the out-of-plane vertical c axis have been applied by artificially modifying the P-P distance, and we find for MnPS$_3$ a clear transition from AFM to FM with the total-energy difference $E_{\text{AFM}} - E_{\text{FM}}$ changing from -93 to 268 meV per formula unit in the presence of a -4% bond-length shortening strain for the P-P distance. Relatively large strains are required to alter the magnetic properties in compounds such as MnPS$_3$, but for other systems such as CrPS$_3$, FePS_3, FePSe$_3$, NiPS$_3$, and VPTe$_3$, the magnetic phase transitions can be achieved for smaller strains as they have relatively smaller total-energy differences between the magnetic phases. We find a particularly sensitive transition near charge neutrality for FePS$_3$, FePSe$_3$, and VPTe$_3$, where strains of the order of $\sim$1% is enough to switch between different magnetic configurations.

V. SUMMARY AND DISCUSSION

In this paper, we have carried out an *ab initio* study of the MPX_3 transition-metal phosphorous trichalcogenide class of two-dimensional materials. We have considered different combinations of 3d metals ($M =$ V, Cr, Mn, Fe, Co, Ni, Cu, Zn) and chalcogens ($X =$ S, Se, Te) in an effort to identify materials that are promising for spintronics based on two-dimensional materials. Our calculations suggest that magnetic phases are common in the single-layer limit of these van der Waals materials, and that the configuration of the magnetic state depends systematically on the transition-metal/ chalcogen element combination. We find that semiconducting Néel antiferromagnetic states are most common, and predict AFM phases for V-, Mn-, Fe-, and Ni-based compounds. A metallic ferromagnetic states is found in Cr-based compounds, and nonmagnetic states are found with both semiconducting and metallic electronic structure, while introduction of U tends to stabilize the AFM magnetic phase. As expected on the basis of the weaker covalent bonds of larger atomic orbitals, we find that for semiconducting antiferromagnetic materials, replacing a smaller chalcogen atom with larger chalcogen atom reduces the energy band gap and, as a consequence, also the difference between the ground-state energies of FM and AFM states. Interestingly, we do not find magnetic states for CoPX_3, even though Co is typically a magnetic atom.

The electronic structures predicted by density functional theory for these materials are sensitive to the choice of exchange-correlation energy functional. For example, there are substantial discrepancies in the predicted densities of states between the standard semilocal GGA, approximations with a local U correction, and hybrid functionals with nonlocal exchange. This sensitivity of the optimized ground-state results to the choice of the approximation scheme makes it desirable to benchmark the results against experiment in order to establish which approximation is most reliably predictive. The fact that the predictions of density functional theory are qualitatively sensitive to the exchange-correlation approximation employed indicates that the MPX_3 compounds are correlated.

An interesting interdependence between magnetic order and atomic structure was found, with typical variations of the order of a few percents in the lattice constant and interatomic bond lengths leading to structural distortions depending on the magnetic configuration of the system. The bond-length variations were traced through M-M, P-P, and P-X bond distances associated with the distortions in the honeycomb array of the transition-metal atoms and the distance between the atomic centers in the $(\text{P}_2 X_6)^{4-}$ bipyramids. We leave for future work the analysis of the role of spin-orbit coupling effects and optical properties arising from lattice symmetry breaking coupled to the onset of magnetism. Sizeable differences between the GGA and the LDA solutions are suggestive of the delicate balance between the different chemical bonds for configuring the optimized structure of these compounds, which in turn are affected by the onset of magnetism. In the antiferromagnetic state, the strength of the exchange interactions is expected to vary inversely with the band gap; approximations that underestimate the band gap will overestimate exchange interaction strengths. We expect that the LDA likely does underestimate band gaps, as it commonly does, and therefore the exchange interactions it implies may well be overestimates. In 2D MPX_3, a variety of different stable and metastable magnetic configurations were found. Semiconducting states with a band gap are typically antiferromagnetic phases in either Néel, zigzag, or stripy configuration and the metallic states

are typically ferromagnetic phases. The critical temperatures for magnetic phases in the single-layer limit are generally expected to be smaller than in the bulk due to the reduction in the number of close-neighbor exchange interactions, although changes in the degree of itinerancy and shifts in relative band positions can also play a role. We analyzed the magnetic phases of the 2D MPX_3 compounds by building an effective model Hamiltonian with exchange coupling parameters extracted by mapping the total energies from our *ab initio* calculations onto an effective classical spin model. The Curie and Néel temperatures T_C, T_N are obtained by using a statistical analysis based on the Metropolis algorithm [64]. The calculated Néel temperatures of the antiferromagnetic compounds have a wide range of variation, ranging between a few to a few-hundred Kelvin.

Control of magnetic phases by varying the electric field in a field-effect transistor device is a particularly appealing strategy for 2D magnetic materials. Our calculations indicate that a transition between antiferromagnetic and ferromagnetic phases can be achieved by inducing carrier densities in 2D MPX_3 compounds that are in the range that can be induced by a field effect. We find that a magnetic phase transition from a FM state to an AFM state can be induced in metallic CrPSe$_3$ and CrPTe$_3$ compounds, which are close to the phase boundary, by gating to large n-type carrier densities. Similarly AFM to FM transitions can be achieved in VPTe$_3$, MnPTe$_3$, and FePS$_3$. For materials exhibiting magnetic phases, we find that using the heavy chalcogen Te can reduce the carrier densities required for magnetic transitions.

The interdependence between the atomic and electronic structure suggests that strains can be employed to tune magnetic phases. We have found that the ground-state magnetic configuration can undergo phase transitions driven by in-plane compression or expansion of the lattice constants or by c-axis pressure. The magnitude of the required strains varies greatly, with values below 1% for compounds such as FePS$_3$, FePSe$_3$, and VPTe$_3$, and larger strains of the order of, or far greater than, 4% are required to trigger a FM-AFM magnetic phase transition in CrPS$_3$ and NiPS$_3$. Phase transitions for even larger strains of the order of $\sim$9% are observed in VPSe$_3$, MnPS$_3$, NiPS$_3$, and NiPSe$_3$, whose nonstrained configuration has a robust gapped antiferromagnetic phase.

Based on our calculations, we conclude that single-layer MPX_3 transition-metal thiophosphates are interesting candidate materials for 2D spintronics. Their properties, including their magnetic transition temperatures, can be adjusted by the application of external strains or by modifying the carrier densities in field-effect transistor devices. The sensitivity of these systems to variations in system parameters, such as composition stoichiometry, details of the interface, and the exchange coupling of the magnetic properties with external fields, offers ample room for future research to seek new functionalities.

ACKNOWLEDGMENTS

[1] K. S. Novoselov, A. K. Geim, S. V. Morozov, D. Jiang, M. I. Katsnelson, I. V. Grigorieva, S. V. Dubonos, and A. A. Firsov, Two-dimensional gas of massless Dirac fermions in graphene, Nature (London) **438**, 197 (2005).

[2] Y. Zhang, Y.-W. Tan, H. L. Stormer, and P. Kim, Experimental observation of the quantum Hall effect and Berry's phase in graphene, Nature (London) **438**, 201 (2005).

[3] K. S. Novoselov, D. Jiang, F. Schedin, T. J. Booth, V. V. Khotkevich, S. V. Morozov, and A. K. Geim, Two-dimensional atomic crystals, Proc. Natl. Acad. Sci. USA **102**, 10451 (2004).

[4] M. Chhowalla, H. S. Shin, G. Eda, L.-J. Li, K. P. Loh, and H. Zhang, The chemistry of two-dimensional layered transition metal dichalcogenide nanosheets, Nat. Chem. **5**, 263 (2013).

[5] L. Britnell, R. M. Ribeiro, A. Eckmann, R. Jalil, B. D. Belle, A. Mishchenko, Y. J. Kim, R. V. Gorbachev, T. Georgiou, S. V. Morozov, A. N. Grigorenko, A. K. Geim, C. Casiraghi, A. H. Castro Neto, and K. S. Novoselov, Strong light-matter interactions in heterostructures of atomically thin films, Science **340**, 1311 (2013).

[6] B. Burk, R. E. Thomson, J. Clarke, and A. Zettl, Surface and bulk charge density wave structure in 1 T-TaS$_2$, Science **257**, 362 (1992).

[7] A. H. Castro Neto, Charge Density Wave, Superconductivity, and Anomalous Metallic Behavior in 2d Transition Metal Dichalcogenides, Phys. Rev. Lett. **86**, 4382 (2001).

[8] R. F. Frindt, Superconductivity in Ultrathin NbSe$_2$ Layers, Phys. Rev. Lett. **28**, 299 (1972).

[9] D. Costanzo, S. Jo, H. Berger, and A. F. Morpurgo, Gate-induced superconductivity in atomically thin MoS$_2$ crystals, Nat. Nanotechnol. **11**, 339 (2016).

[10] L. J. de Jongh, *Magnetic Properties of Layered Transition Metal Compounds* (Springer, Netherlands, 1990).

[11] Y. Ma, Y. Dai, M. Guo, C. Niu, Y. Zhu, and B. Huang, Evidence of the existence of magnetism in pristine VX$_2$ monolayers (X = S, Se) and their strain-induced tunable magnetic properties, ACS Nano **6**, 1695 (2012).

[12] S. Lebegue, T. Björkman, M. Klintenberg, R. M. Nieminen, and O. Eriksson, Two-Dimensional Materials from Data Filtering and *Ab Initio* Calculations, Phys. Rev. X **3**, 031002 (2013).

[13] B. Siberchicot, S. Jobic, V. Carteaux, P. Gressier, and G. Ouvrard, Band structure calculations of ferromagnetic chromium tellurides CrSiTe$_3$ and CrGeTe$_3$, J. Phys. Chem. **100**, 5863 (1996).

[14] M.-W. Lin, H. L. Zhuang, J. Yan, T. Z. Ward, A. A. Puretzky, C. M. Rouleau, Z. Gai, L. Liang, V. Meunier, B. G. Sumpter,

P. Ganesh, P. R. C. Kent, D. B. Geohegan, D. G. Mandrus, and K. Xiao, Ultrathin nanosheets of $CrSiTe_3$: A semiconducting two-dimensional ferromagnetic material, J. Mater. Chem. C **4**, 315 (2016).

[15] T. J. Williams, A. A. Aczel, M. D. Lumsden, S. E. Nagler, M. B. Stone, J.-Q. Yan, and D. Mandrus, Magnetic correlations in the quasi-2D semiconducting ferromagnet $CrSiTe_3$, Phys. Rev. B **92**, 144404 (2015).

[16] X. Chen, J. Qi, and D. Shi, Strain-engineering of magnetic coupling in two-dimensional magnetic semiconductor crsite3: Competition of direct exchange interaction and superexchange interaction, Phys. Lett. A **379**, 60 (2015).

[17] L. D. Casto, A. J. Clune, M. O. Yokosuk, J. L. Musfeldt, T. J. Williams, H. L. Zhuang, M.-W. Lin, K. Xiao, R. G. Hennig, B. C. Sales, J.-Q. Yan, and D. Mandrus, Strong spin-lattice coupling in $CrSiTe_3$, APL Mater. **3**, 041515 (2015).

[18] N. Sivadas, M. W. Daniels, R. H. Swendsen, S. Okamoto, and D. Xiao, Magnetic ground state of semiconducting transition-metal trichalcogenide monolayers, Phys. Rev. B **91**, 235425 (2015).

[19] H. L. Zhuang, Y. Xie, P. R. C. Kent, and P. Ganesh, Computational discovery of ferromagnetic semiconducting single-layer $CrSnTe_3$, Phys. Rev. B **92**, 035407 (2015).

[20] M. A. McGuire, H. Dixit, V. R. Cooper, and B. C. Sales, Coupling of crystal structure and magnetism in the layered, ferromagnetic insulator CrI_3, Chem. Mater. **27**, 612 (2015).

[21] W. B. Zhang, Q. Qu, P. Zhu, and C. H. Lam, Robust intrinsic ferromagnetism and half semiconductivity in stable two-dimensional single-layer chromium trihalides, J. Mater. Chem. C **3**, 12457 (2015).

[22] X. Li, X. Wu, and J. Yang, Half-metallicity in $MnPSe_3$ exfoliated nanosheet with carrier doping, J. Am. Chem. Soc. **136**, 11065 (2014).

[23] X. Li, T. Cao, Q. Niu, J. Shi, and J. Feng, Coupling the valley degree of freedom to antiferromagnetic order, Proc. Natl. Acad. Sci. USA **110**, 3738 (2013).

[24] R. Brec, Review on structural and chemical properties of transition metal phosphorous trisulfides MPS_3, Solid State Ionics **22**, 3 (1986).

[25] A. R. Wildes, B. Roessli, B. Lebech, and K. W. Godfrey, Spin waves and the critical behavior of the magnetization in $MnPS_3$, J. Phys.: Condens. Matter **10**, 6417 (1998).

[26] E. Prouzet, G. Ouvrard, and R. Brec, Structure determination of $ZnPS_3$, Mater. Res. Bull. **21**, 195 (1986).

[27] G. Ouvrard, R. Brec, and J. Rouxel, Structural determination of some MPS_3 layered phases (M = Mn, Fe, Co, Ni and Cd), Mater. Res. Bull. **20**, 1181 (1985).

[28] G. Ouvrard, R. Freour, R. Brec, and J. Rouxel, A mixed valence compound in the two dimensional MPS_3 family: $V_{0.78}PS_3$ structure and physical properties, Mater. Res. Bull. **20**, 1053 (1985).

[29] P. A. Joy and S. Vasudevan, Infrared (700-100 cm^{-1}) vibrational spectra of the layered transition metal thiophosphates, MPS_3, (M = Mn, Fe AND Ni), J. Phys. Chem. Solids. **54**, 343 (1993).

[30] K. C. Rule, Magnetic ordering in the two dimensional antiferromagnet $FePS_3$, Ph.D. thesis, School of Physics and Material Engineering, Monash University, Australia, 2004.

[31] E. Ressouche, M. Loire, V. Simonet, R. Ballou, A. Stunault, and A. Wildes, Magnetoelectric $MnPS_3$ as a candidate for ferrotoroidicity, Phys. Rev. B **82**, 100408(R) (2010).

[32] K. Kurosawa, S. Saito, and Y. Yamaguchi, Neutron Diffraction Study on $MnPS_3$ and $FePS_3$, J. Phys. Soc. Jpn. **52**, 3919 (1983).

[33] W. Klingen, G. Eulenberger, and H. Hahn, About Hexathio- and Hexaselenohypodiphosphate type $M_2^{II}P_2X_6$, Nat. Sci. **55**, 229 (1968).

[34] N. Kurita and K. Nakao, Band structure of magnetic layered semiconductor $NiPS_3$, J. Phys. Soc. Jpn. **58**, 232 (1989).

[35] K. C. Rule, G. J. McIntyre, S. J. Kennedy, and T. J. Hicks, Single-crystal and powder neutron diffraction experiments on $FePS_3$: Search for the magnetic structure, Phys. Rev. B **76**, 134402 (2007).

[36] N. Kurita and K. Nakao, Band structures and physical properties of magnetic layered semiconductors MPS_3, J. Phys. Soc. Jpn. **58**, 610 (1989).

[37] G. Le Flem, R. Brec, G. Ouvard, A. Louisy, and P. Segransan, Magnetic interactions in the layer compunds MPX_3 (M=Mn, Fe, Ni;X=S, Se), J. Phys. Chem. Solids **43**, 455 (1982).

[38] D. J. Goossens, Dipolar anisotropy in quasi-2D honeycomb antiferromagnet $MnPS_3$, Eur. Phys. J. B **78**, 305 (2010).

[39] N. Chandrasekharan and S. Vasudevan, Magnetism, exchange and crystal field parameters in the orbitally unquenchedlsing antiferromagnet $FePS_3$, Pramana: J. Phys. **43**, 21 (1994).

[40] P. Jeevanandam and S. Vasudevan, Magnetism in $MnPSe_3$: A layered $3d^5$ antiferromagnet with unusually large XY anisotropy, J. Phys.: Condens. Matter **11**, 3563 (1999).

[41] P. A. Joy and S. Vasudevan, Magnetism in the layered transition-metal thiophosphates MPS_3 (M =Mn, Fe, and Ni), Phys. Rev. B **46**, 5425 (1992).

[42] A. R. Wildes, K. C. Rule, R. I. Bewley, M. Enderle, and T. J. Hicks, The magnon dynamics and spin exchange parameters of $FePS_3$, J. Phys.: Condens. Matter **24**, 416004 (2012).

[43] A. R. Wildes. S. J. Kennedy, and T. J. Hicks, True two-dimensionalmagnetic ordering in $MnPS_3$, J. Phys.: Condens. Matter **6**, L335 (1994).

[44] J. Liu, X.-B. Li, D. Wang, W.-M. Lau, P. Peng, and L.-M. Liu, Diverse and tunable electronic structures of single-layer metal phosphorus trichalcogenides for photocatalytic water splitting, J. Chem. Phys. **140**, 054707 (2014).

[45] C.-T. Kuo, M. Neumann, K. Balamurugan, H. J. Park, S. Kang, H. W. Shiu, J. H. Kang, B. H. Hong, M. Han, T. W. Noh, and J.-G. Park, Exfoliation and Raman spectroscopic fingerprint of few-layer NiPS3 Van der Waals Crystals, Sci. Rep. **6**, 20904 (2016).

[46] C.-T. Kuo, K. Balamurugan, H. W. Shiu, H. J. Park, S. Sinn, M. Neumann, M. Han, Y. J. Chang, C.-H. Chen, H.-D. Kim, J.-G. Park, and T. W. Noh, The energy band alignment at the interface between mechanically exfoliated few-layer NiPS3 nanosheets and ZnO, Curr. Appl. Phys. **16**, 404 (2016).

[47] J.-U. Lee, S. Lee, J. H. Ryoo, S. Kang, T. Y. Kim, P. Kim, C.-H. Park, J.-G. Park, and H. Cheong, Ising-type magnetic ordering in atomically thin $FePS_3$, arXiv:1608.04169.

[48] K. Z. Du, X. Z. Wang, Y. Liu, P. Hu, M. I. B. Utama, C. K. Gan, Q. H. Xiong, and C. Kloc, Weak Van der Waals stacking, wide-range band gap, and Raman study on ultrathin layers of metal phosphorus trichalcogenides, ACS Nano. **10**, 1738 (2016).

[49] A. R. Wildes, V. Simonet, E. Ressouche, G. J. McIntyre, M. Avdeev, E. Suard, S. A. J. Kimber, D. Lançon, G. Pepe, B. Moubaraki, and T. J. Hicks, Magnetic structure of the quasi-two-dimensional antiferromagnet $NiPS_3$, Phys. Rev. B **92**, 224408 (2015).

[50] R. Brec, D. M. Schleigh, G. Ouvrard, A. Louisy, and J. Rouxel, Physical properties of lithium intercalation compounds of the

layered transition chalcogenophosphates, Inorg. Chem. **18**, 1814 (1979).

[51] P. J. S. Foot, T. Katz, S. N. Patel, B. A. Nevett, A. R. Piercy, and A. A. Balchin, The structures and conduction mechanisms of lithium-intercalated and lithium-substituted nickel phosphorus trisulphide (NiPS$_3$), and the use of the material as a secondary battery electrode, Phys. Stat. Sol. A **100**, 11 (1987).

[52] P. J. S. Foot and B. A. Nevett, Electronic conduction in p- and n-Type NiPS$_3$, Phys. Stat. Sol. A **93**, 283 (1986).

[53] R. Clement, Ion-exchange intercalation into the MPS$_3$ layered compounds: Design of nanocomposites with unusual magnetic, electrical, and nonlinear optical properties, in *Hybrid Organic-Inorganic Composites*, ACS Symposium Series 585, edited by J. E. Mark, C. Y.-C. Lee, and P. A. Bianconi (American Chemical Society, Washington, DC, 1995), Chap. 4, pp. 29–42.

[54] Y. Mathey, R. Clement, J. P. Audiere, O. Poizat, and C. Sourisseau, Structural, vibrational and conduction properties of a new class of layer-type MPS$_3$ compounds, $Mn^{II}_{1-x}M^{I}_{2x}PS_3$ (M^I = Cu, Ag), Solid State Ionics **9–10**, 459 (1983).

[55] P. Giannozzi, S. Baroni, N. Bonini, M. Calandra, R. Car, C. Cavazzoni, D. Ceresoli, G. L. Chiarotti, M. Cococcioni, I. Dabo, A. D. Corso, S. de Gironcoli, S. Fabris, G. Fratesi, R. Gebauer, U. Gerstmann, C. Gougoussis, A. Kokalj, M. Lazzeri, L. Martin-Samos, N. Marzari, F. Mauri, R. Mazzarello, S. Paolini, A. Pasquarello, L. Paulatto, C. Sbraccia, S. Scandolo, G. Sclauzero, A. P. Seitsonen, A. Smogunov, P. Umari, and R. M. Wentzcovitch, QUANTUM ESPRESSO: A modular and open-source software project for quantum simulations of materials, J. Phys.: Condens. Matter **21**, 395502 (2009).

[56] J. P. Perdew, K. Burke, and M. Ernzerhof, Generalized Gradient Approximation Made Simple, Phys. Rev. Lett. **77**, 3865 (1996).

[57] S. Grimme, Semiempirical GGA-type density functional constructed with a long-range dispersion correction, J. Comp. Chem. **27**, 1787 (2006).

[58] J. P. Perdew and A. Zunger, Self-interaction correction to density-functional approximations for many-electron systems, Phys. Rev. B **23**, 5048 (1981).

[59] N. Marom, J. Bernstein, J Garel, A. Tkatchenko, E. Joselevich, L. Kronik, and O. Hod, Stacking and Registry Effects in Layered Materials: The Case of Hexagonal Boron Nitride, Phys. Rev. Lett. **105**, 046801 (2010).

[60] J. Heyd, G. Scuseria, and M. Ernzerhof, Hybrid functionals based on a screened Coulomb potential, J. Chem. Phys. **118**, 8207 (2003).

[61] See Supplemental Material at http://link.aps.org/supplemental/10.1103/PhysRevB.94.184428 for the lattice structures, band structures, the associated density of states and the orbital projected density of states (PDOS) calculated for self-consistently

converged magnetic configurations with total-energy local minima with the energy origin $E = 0$ placed at the valence-band edge for gapped bands. The carrier-density-dependent magnetic phase transition is calculated using a finite on-site repulsion $U = 4$ eV on the GGA+D2. We also obtain the magnetization as a function of temperature through the Metropolis Monte Carlo simulation in a 32×64 superlattice.

[62] J. Chaloupka, G. Jackeli, and G. Khaliullin, Zigzag Magnetic Order in the Iridium Oxide Na$_2$IrO$_3$, Phys. Rev. Lett. **110**, 097204 (2013).

[63] N. Metropolis, A. W. Rosenbluth, M. N. Rosenbluth, A. H. Teller, and E. Teller, Equation of state calculations by fast computing machines, J. Chem. Phys. **21**, 1087 (1953).

[64] M. E. J. Newman and G. T. Barkema, *Monte Carlo Methods in Statistical Physics* (Clarendon Press, Oxford, 1999).

[65] D. P. Landauand and K. Binder, *Monte Carlo Simulations in Statistical Physics* (Cambridge University Press, Cambridge, 2000).

[66] D. P. Landau, S.-H. Tsai, and M. Exler, A new approach to Monte Carlo simulations in statistical physics: Wang-Landau sampling, Am. J. Phys. **72**, 1294 (2004).

[67] F. Matsukura, Y. Tokura, and H. Ohno, Control of magnetism by electric fields, Nat. Nanotechnol. **10**, 209 (2015).

[68] H. Ohno, D. Chiba, F. Matsukura, T. Omiya, E. Abe, T. Dietl, Y. Ohno, and K. Ohtani, Electric-field control of ferromagnetism, Nature (London) **408**, 944 (2000).

[69] M. Endo, S. Kanai, S. Ikeda, F. Matsukura and H. Ohno, Electric-field effects on thickness dependent magnetic anisotropy of sputtered MgO/Co$_{40}$Fe$_{40}$B$_{20}$/Ta structures, App. Phys. Lett. **96**, 212503 (2010).

[70] N. Levy, S. A. Burke, K. L. Meaker, M. Panlasigui, A. Zettl, F. Guinea, A. H. Castro Neto, and M. F. Crommie, Strain-induced pseudo-magnetic fields greater than 300 tesla in graphene nanobubbles, Science **329**, 544 (2010).

[71] B. Hunt, J. D. Sanchez-Yamagishi, A. F. Young, M. Yankowitz, B. J. LeRoy, K. Watanabe, T. Taniguchi, P. Moon, M. Koshino, P. Jarillo-Herrero, and R. C. Ashoori, Massive dirac fermions and hofstadter butterfly in a van der Waals heterostructure, Science **340**, 1427 (2013).

[72] C. R. Woods, L. Britnell, A. Eckmann, R. S. Ma, J. C. Lu, H. M. Guo, X. Lin, G. L. Yu, Y. Cao, R. V. Gorbachev, A. V. Kretinin, J. Park, L. A. Ponomarenko, M. I. Katsnelson, Yu. N. Gornostyrev, K. Watanabe, T. Taniguchi, C. Casiraghi, H.-J. Gao, A. K. Geim, and K. S. Novoselov, Commensurate-incommensurate transition in graphene on hexagonal boron nitride, Nat. Phys. **10**, 451 (2014).

[73] J. Jung, A. M. DaSilva, A. H. MacDonald, and S. Adam, Origin of band gaps in graphene on hexagonal boron nitride, Nat. Commun. **6**, 6308 (2015).